RSC Advances

PAPER

View Article Online
View Journal | View Issue

Cite this: *RSC Adv.*, 2024, **14**, 33619

Unraveling fundamental characteristics of $Na_2Mg_3Cl_8$ as a solid-state electrolyte for Na-ion batteries†

Yohandys A. Zulueta, [a] Jose R. Fernández-Gamboa, [a] Thi Viet Bac Phung,[b] My Phuong Pham-Ho[cd] and Minh Tho Nguyen*[ef]

Received 8th September 2024
Accepted 7th October 2024

DOI: 10.1039/d4ra06490a

rsc.li/rsc-advances

In this theoretical study, we harnessed advanced atomistic computations to unravel several features of $Na_2Mg_3Cl_8$, an unexplored but promising chloride compound for solid-state electrolytes in Na-batteries. First, $Na_2Mg_3Cl_8$ exhibits an insulating behavior, characterized by an energy gap of ~5 eV, arising from the hybridization of [NaCl] trigonal prismatic and [$MgCl_6$] octahedral units. Second, the compound possesses mechanical stability and ductility, which render it suitable for practical fabrication. Improved electrolyte/electrode contact can reduce resistance and enhance battery performance. The electrochemical performance of $Na_2Mg_3Cl_8$ involves an open cell voltage of 1.2 V and a theoretical capacity of 133 mA h g^{-1}. Finally, its transport characteristics include low activation energy for diffusion and conduction as well as a remarkable room-temperature conductivity of 1.26 mS cm^{-1}, comparable to those of current superionic conductors.

1. Introduction

Sodium-ion batteries (NIBs) currently hold significant importance owing to their cost-effectiveness, sustainability, safety, performance, scalability, and diverse applications.[1–7] As an alternative to lithium-ion batteries, NIBs offer several advantages as they utilize abundant and low-cost materials, making them economically more viable.[1–7] Additionally, NIBs exhibit energy-efficient power delivery, fast charging, stability across extreme temperatures, and safety against overheating or thermal runaway.[1–9] Their emergence represents a key step toward efficient and sustainable energy storage.[1–14]

Although NIBs have garnered attention as a cost-effective alternative to lithium-ion batteries (LIBs) for large-scale energy storage, their lower energy density than that of LIBs necessitates further intensive research and innovation.[5–9] One critical component in NIBs is the solid electrolyte, which plays a pivotal role in transferring charge carriers between both positive and negative electrodes. Solid-state electrolytes (SSEs) offer a higher energy density than liquid counterparts, making them more suitable for NIBs. However, the current SSEs suffer from several limitations such as low ionic conductivity, narrow electrochemical stability window, and poor contact with electrodes.[10–14]

In this context, theoretical computations for discovering new solid-state electrolytes (SSEs) for sodium-ion batteries are pivotal.[15–19] These computational methods provide us with insights into fundamental properties and mechanisms associated with SSEs, thereby accelerating their development and implementation. Current computational techniques include atomistic first-principles calculations, molecular dynamics simulations and force field approaches.[15,20,21] Results derived from advanced atomistic simulations can guide the design of SSEs with high ion diffusivity, chemical stability, and a wide electrochemical stability window, ultimately advancing all-solid-state battery technology.[15–19]

As potential materials, halide-based sodium solid-state electrolytes offer several key benefits. First, they exhibit high voltage stability and air stability, which make them suitable for cell manufacturing. Additionally, these electrolytes possess decent room temperature ionic conductivity, which is crucial for efficient ion transport within batteries.[22–25] They are also compatible with oxide cathode materials, ensuring good performance when paired with employed electrodes. Furthermore, halide solid electrolytes provide excellent chemical

[a]*Departamento de Física, Facultad de Ciencias Naturales y Exactas, Universidad de Oriente, CP 90500, Santiago de Cuba, Cuba*

[b]*Center for Environmental Intelligence, College of Engineering and Computer Science, VinUniversity, Hanoi, 10000 Vietnam*

[c]*Faculty of Chemical Engineering, Ho Chi Minh City University of Technology (HCMUT), 268 Ly Thuong Kiet Street, District 10, Ho Chi Minh City, 70000 Vietnam*

[d]*Vietnam National University Ho Chi Minh City, Linh Trung, Thu Duc City, Ho Chi Minh City, 70000 Vietnam*

[e]*Laboratory for Chemical Computation and Modeling, Institute for Computational Science and Artificial Intelligence, Van Lang University, Ho Chi Minh City, 70000 Vietnam. E-mail: minhtho.nguyen@vlu.edu.vn*

[f]*Faculty of Applied Technology, School of Technology, Van Lang University, Ho Chi Minh City, 70000 Vietnam*

† Electronic supplementary information (ESI) available. See DOI: https://doi.org/10.1039/d4ra06490a

stability, an essential requirement for maintaining battery performance over multiple charge–discharge cycles. Their robustness helps prevent degradation and ensures long-term reliability. Lastly, their scalability makes them a viable option for large-scale battery manufacturing, which is advantageous for commercial applications. These considerations lead to the motivation for intensive ongoing research in this field.[22–25]

Advanced atomistic simulations were previously carried out to assess the key features of the Na_6MgCl_8 rock-salt material.[25,26] It was found that Na_6MgCl_8 is an insulating material with an energy gap of ~5 eV, and it exhibits mechanical stability and ductility. Theoretical simulations predicted that the Zn^{2+} ion is the most suitable divalent dopant that enhances the defect characteristics and transport properties of the Na_6MgCl_8 structure.[26] Indeed, the Na transport properties were found to be notably improved upon the doping of Na_6MgCl_8 with Ba^{2+} and Zn^{2+} ions.[26] Expanding the study to Na_6MCl_8 compounds, where M = Ca^{2+}, Ba^{2+}, Zn^{2+} and Sr^{2+}, we observed some remarkable properties. These include lower energy gap than the reported values for Na_6MgCl_8 (which has an energy gap of 4.1–4.6 eV). All relevant structures are mechanically stable and ductile, ensuring compatibility with electrodes. Additionally, a three-dimensional migration pathway was predicted. The Na_6BaCl_8 structure possesses the lowest values of defect formation energies and the highest conductivity at 250 K.[25]

Na_6MgCl_8 compound having the same type of atoms (Na, Mg and Cl) was investigated in earlier studies as a $Na_2Mn_3Cl_8$ isostructural motif in the search for the crystal structure of Na_6MnCl_8 and $Na_2Mn_3Cl_8$ lattice structures.[27] There are no previous works reporting the physicochemical properties and technological applications of $Na_2Mg_3Cl_8$. In this context, an exploration of the inherent properties and thereby the possible application of $Na_2Mg_3Cl_8$ compound in battery technology is of interest. Bearing in mind the importance of theoretical computations for the rapid delivery of properties of materials, the aim of the present work is to reveal the under-evaluated battery properties of the $Na_2Mg_3Cl_8$ material with the aid of advanced atomistic simulations. In this work, by integrating density functional theory (DFT), static simulations, defect energetics, and bond valence site energy (BVSE) computations, for the first time, we have elucidated the structural, electronic, mechanical, and transport properties of the quasi-unexplored $Na_2Mg_3Cl_8$ compound. The predicted properties suggest that $Na_2Mg_3Cl_8$ is a promising candidate for use as a solid-state electrolyte in current or future sodium-ion batteries.

2. Computational methodology

DFT calculations were performed using the CASTEP code to determine the structural, electronic and mechanical properties of the $Na_2Mg_3Cl_8$ compound.[28] The GGA-PBESOL exchange–correlation functional within the generalized gradient approximation was employed.[29] Ultrasoft pseudopotentials with a plane-wave energy cutoff of 830 eV were utilized. Specifically, the pseudoatomic functions for Na-$2s^2 2p^6 3s^1$, Mg-$2p^6 3s^2$ and Cl-$3s^2 3p^5$ in reciprocal space represent the electronic configurations of the constituent atoms.

For electronic structure computations and geometry optimizations, we set the convergence thresholds as follows: a total energy change of 5×10^{-6} eV per atom and maximum force, stress, and atomic displacements of 10^{-2} eV Å^{-1}, 2×10^{-2} GPa, and 5×10^{-4} Å, respectively. Additionally, a $4 \times 4 \times 4$ k-point mesh following the Monkhorst–Pack method samples the Brillouin zone.[30]

To perform force field-based computations, the General Utility Lattice Program (GULP) was employed,[31] in which the potential parameters (force field) are derived from prior studies, describing both long-range and short-range interactions.[26,32,33] Specifically, the Buckingham formulation governs short-range interactions, while long-range interactions are treated as coulombic forces, where only the charge and interatomic distance contribute to the long-range potential energy. Together with the force field (FF), the shell model accounts for ionic polarization, where each ion is approximated as a positively charged core connected to a negatively charged shell by a spring, and the sum of the core–shell charges yield the formal charge of the polarizable species.[34]

For defect calculations, the Mott–Littleton method was employed,[35] in which the crystal structure is divided into two concentric spherical regions with radii $R1$ and $R2$, where $R1 < R2$. The inner sphere contains the isolated defect or defect cluster, positioned where the interaction with the local structure is strong. Meanwhile, region $R2$ is treated using a quasi-continuum approximation. We adopted specific values of $R1$ = 13 Å and $R2$ = 27 Å to ensure smooth convergence in simulations. Geometry optimizations and defect energetics computations utilized the Broyden–Fletcher–Goldfarb–Shanno (BFGS) algorithm,[31,36] which is a widely applied technique to explore defect formation in various solid-state materials.[15,20,21,32,37]

Furthermore, the BVSE offers a straightforward and effective approach for determining diffusion paths and activation energies in diffusion and conduction processes.[16–19] This method identifies mobile cations based on regions of low bond valence site energy. Specifically, the bond length between a cation A and an anion (L_{A-x}) is evaluated using the tabulated empirical parameters $L_{0,A-x}$ and b_{A-x}, which are related to individual bond valences (1).

$$s_{A-x} = \exp[(L_{0,A-x} - L_{A-x})/b_{A-x}] \quad (1)$$

The bond valence site energy of a cation A [$E_{BVSE}(A)$] is evaluated in a similar way to the Morse empirical potentials[16–19] by adding the coulombic repulsive term (E_r) of the mobile A ion with respect to other immobile ions (eqn (2)).

$$E_{BVSE}(A) = \sum_x D_0 \left[\sum_{i=1}^{N} \left[(S_{A-X}/S_{\min A-X})^2 - 2S_{A-X}/S_{\min A-X} \right] \right] + E_r \quad (2)$$

The softBV-GUI, code which serves as a bond valence pathway analyser, was employed for computing E_{BVSE}(Na). The necessary parameters from eqn (2) were seamlessly integrated

into the softBV-GUI code. Specifically, when analysing E_{BVSE}(Na) coulombic repulsions between mobile sodium ions (Na^+) and immobile Mg^{2+} cations were considered. Coulombic attraction interactions were included into the Morse-type attraction terms. For further insights into the bond valence approach, we refer readers to the recent relevant references.[16–19,38]

3. Results and discussion

3.1 Structural and electronic properties of the $Na_2Mg_3Cl_8$ structure

Fig. 1 displays the unit cell in the hexagonal representation of the $Na_2Mg_3Cl_8$ lattice structure. Compared to Na_6MgCl_8, while the chloride $Na_2Mg_3Cl_8$ crystallizes into a hexagonal lattice structure (space group $R\bar{3}m$), Na_6MgCl_8 adopts a cubic $Fm\bar{3}m$ space group with a lattice parameter of $a = 11.085$ Å. Na_6MgCl_8 has a rock-salt structure with four primitive cells, whereas $Na_2Mg_3Cl_8$ has lattice parameters of $a = 7.355$ Å and $c = 19.511$ Å, possessing three primitive cells in its hexagonal representation.[27] In the $Na_2Mg_3Cl_8$ structure, while Na^+ ions are six-coordinated with Cl^- ions, resulting in trigonal prismatic hybridization, Mg^{2+} cations are also six-coordinated with Cl^- anions, forming an octahedron.[27] Notably, $Na_2Mg_3Cl_8$ offers more accessible sites for Na^+ ions, making it interesting for Na^+ storage and migration.[27]

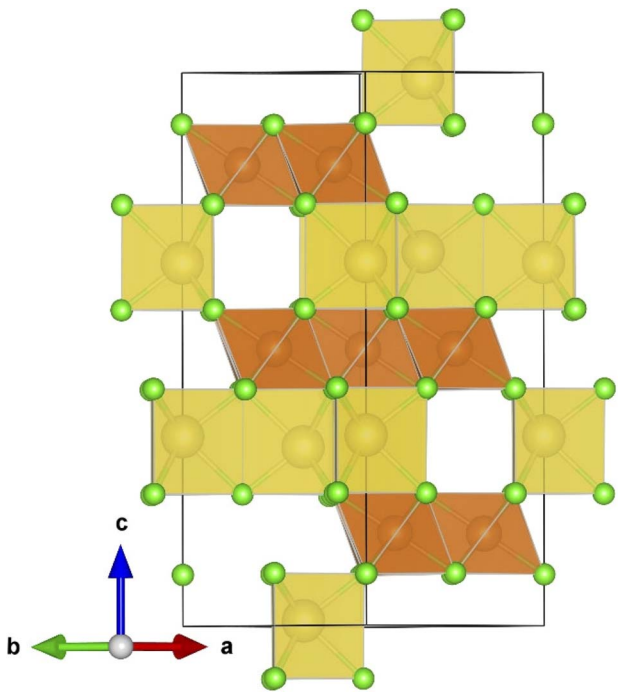

Fig. 1 Hexagonal representation of the $Na_2Mg_3Cl_8$ lattice structure ($R\bar{3}m$ space group). Yellow prisms represent the [NaCl] polyhedron, light brown the [$MgCl_6$] octahedron and green balls Cl^- ions.

Table 1 shows the results of the cell parameters obtained by DFT and force field computations. We observed that the *a*-cell parameter obtained from the FF method was underestimated by 3.7%, while the *c*-parameter was underestimated by 2.6% with respect to available experimental data.[27] Conversely, results from DFT computations exhibit a low overestimation as compared to the literature values.[27] Commonly DFT computations tend to overestimate the lattice parameters, whereas the force field method tends to underestimate these values. In this study, the differences between the computed values with the experiment are small. Consequently, both approaches are suitable for reproducing the cell parameters of $Na_2Mg_3Cl_8$.

Exploration of electronic properties is of vital importance to decide the applicability of a compound as a battery material. An electrode material needs to be a good electric conductor to facilitate charge transfer during battery operation. Fig. 2 depicts the band structure of $Na_6Mg_3Cl_8$ in the equilibrium ground state. The valence bands are located between −3.5 eV and the Fermi level (0 eV reference), while the conduction bands lie between 4.9 and 16 eV. Many electrons lie at the top valence bands at the Γ-point (G), which can be passed to the bottom of the conduction band along the Γ-point. The calculated energy gap value of $E_g = 4.9$ eV is similar to that of 5.1 eV previously reported for Na_6MgCl_8 compound.[26] This closely aligns with the criteria for considering SSEs as these compounds exhibit minimal electronic conduction. In view of the usual underestimation of DFT calculations and the lack of experimental results, the value of $E_g = 4.9$ eV should be considered as a lower bound.[39]

Fig. 2b shows the density of states of $Na_6Mg_3Cl_8$. The valence band is dominated by Cl^- ions and the conduction band by Mg^{2+} cations (Fig. 2b); Na^+-DOS has lower contributions to both valence and conduction bands. These results agree well with the [NaCl] trigonal prismatic and [$MgCl_6$] octahedral hybridization, defining the $Na_2Mg_3Cl_8$ lattice structure.

3.2 Defect chemistry in $Na_2Mg_3Cl_8$ structure

Intrinsic defects significantly influence the transport properties of materials. Notably, the Schottky defect type is prevalent in conducting materials. The Schottky formation mechanism is typically described using three distinct schemes. The first scheme, expressed in Kröger–Vink notation,[40] is described by eqn (3)

$$2Na^{\times}_{Na} + 3Mg^{\times}_{Mg} + 8Cl^{\times}_{Cl} \rightarrow 2V^{'}_{Na} + 6V^{''}_{Mg} + 8V^{\cdot}_{Cl} + Na_2Mg_3Cl_8 \quad (3)$$

Table 1 Results of cell parameters of the optimized $Na_2Mg_3Cl_8$ lattice structure ($R\bar{3}m$ space group) derived from different approaches

	Methods		
Cell parameters (Å)	Force fields	DFT	Experimental (ref. 27)
a	7.086 (−3.7%)	7.377 (+0.3%)	7.355
c	19.000 (−2.6%)	19.601 (+0.5%)	19.511

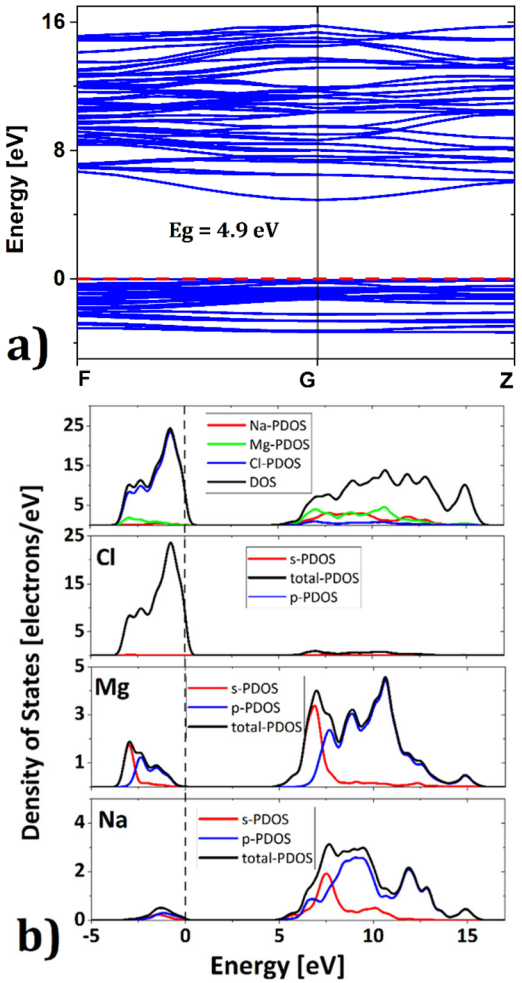

Fig. 2 (a) Band gap and (b) density of states of the $Na_2Mg_3Cl_8$ structure; red and black dashed lines represent the Fermi level.

where $Na_{Na}^{\times}$, $M_M^{\times}$ and $Cl_{Cl}^{\times}$ represent the host ions occupying its respective atomic position at the $Na_2Mg_3Cl_8$ lattice structure, while $V_{Na}^{'}$, $V_M^{''}$ and $V_{Cl}^{\cdot}$ symbolize an Na-, Mg- and Cl-vacancy, respectively. In this sense, eqn (3) describes the full Schottky defect formation mechanism. The formation of NaCl Schottky defect is described by eqn (4),

$$Na_{Na}^{\times} + Cl_{Cl}^{\times} \rightarrow V_{Na}^{'} + V_{Cl}^{\cdot} + NaCl \quad (4)$$

resulting in a stoichiometric $Na_{2-x}Mg_3Cl_{8-x}$ composition, while the formation of the $MgCl_2$ Schottky defect is given by eqn (5),

$$Mg_{Mg}^{\times} + 2Cl_{Cl}^{\times} \rightarrow V_{Mg}^{''} + 2V_{Cl}^{\cdot} + MgCl_2 \quad (5)$$

which leads to the stoichiometric $Na_2Mg_{3-x}Cl_{8-2x}$ formula. Because the Frenkel type defects are commonly unfavorable,[20,21,32] they are not considered in the present work.

The solution energy (E_s) is then computed as (eqn (6)–(8)) follows

$$E_s = \frac{1}{3}\left(2E_{vac}^{Na} + 3E_{vac}^{Mg} + 8E_{vac}^{Cl} + E_L^{Na_2Mg_3Cl_8}\right) \quad (6)$$

$$E_s = \frac{1}{2}\left(E_{vac}^{Na} + E_{vac}^{Cl} + E_L^{NaCl}\right) \quad (7)$$

$$E_s = \frac{1}{2}\left(E_{vac}^{Mg} + 2E_{vac}^{Cl} + E_L^{MgCl_2}\right) \quad (8)$$

in relation to eqn (3)–(5), respectively, where E_{vac}^{Na}, E_{vac}^{Mg}, and E_{vac}^{Cl} denote the Na-, Mg- and Cl-vacancy energy, while $E_L^{Na_2Mg_3Cl_8}$, E_L^{NaCl} and $E_L^{MCl_2}$ symbolize the lattice energy of $Na_2Mg_3Cl_8$, NaCl and $MgCl_2$ compounds, respectively.

Table 2 collects the calculated results of defect energetics computations. The lowest vacancy formation energy corresponds to the Na^+ vacancy of 5.2 eV per vacancy, followed by Cl^- vacancy (5.9 eV per vacancy). Compared to the reported vacancy formation energy in Na_6MgCl_8 (5.2 and 5.4 eV per vacancy for Na^+ and Cl^- vacancy, respectively),[26] the basic vacancy formation energies are comparable to each other between these chloride structures (including the Mg^{2+} vacancy formation energy). On the other hand, it has been reported that the Na^+ and Cl^- vacancies are the most common defect types that appear in chloride structures.[23–26,32] This result confirms that the observation mentioned above is also valid for the $Na_2Mg_3Cl_8$ structure.

Table 2 also includes the results of Schottky solution energy obtained from eqn (6)–(8). The lowest Schottky formation energy corresponds to the NaCl defect type (1.49 eV per defect), followed by the $MgCl_2$-Schottky and full $Na_2Mg_3Cl_8$-Schottky schemes. Again, this result suggests that the most abundant defect type in this structure must be the NaCl-Schottky type, with a minor influence of the $MgCl_2$-Schottky scheme. The NaCl-Schottky type involves $V_{Na}^{'}$ formation, which determines the conduction mechanism in this structure. In comparison to NaCl-Schottky in the Na_6MgCl_8 structure (being 1.26 eV per defect),[26] the solution energy in $Na_2Mg_3Cl_8$ appears to be similar, which seemingly confirms that this Schottky defect type is responsible for the transport properties in this material.

3.3 Mechanical properties of $Na_2Mg_3Cl_8$ structure

Accurate information on mechanical properties is of crucial importance when selecting materials for use as electrodes or electrolytes in batteries.[41–43] Ensuring mechanical stability involves achieving a moderate Young's modulus to facilitate desirable contact between a solid electrolyte and the electrodes,

Table 2 Schottky solution energies derived from eqn (6)–(8), including the lattice energy of $Na_2Mg_3Cl_8$, NaCl and $MgCl_2$, and the vacancy energy of the constituent ions

Lattice energy (eV per fu)			Vacancy formation energy (eV per vacancy)		
$E_L^{MCl_2}$	$E_L^{Na_2Mg_3Cl_8}$	E_L^{NaC}	E_{vac}^{Mg}	E_{vac}^{C1}	E_{vac}^{Na}
−26.52	−95.68	−8.10	21.80	5.88	5.20

Schottky solution energy (eV per defect)		
NaCl	$MgCl_2$	$Na_2Mg_3Cl_8$
1.49	3.52	9.06

thereby preventing the formation of undesirable voids and cracks that could impact long-range transport properties and the battery life.[41–43] The mechanical behavior of a crystalline structure follows Hooke's law and is described by the elastic constant matrix (C_{ij}), eqn (9).

$$C_{ij} = \frac{1}{V_0}\left(\frac{\partial^2 E}{\partial \varepsilon_i \partial \varepsilon_j}\right) \quad (9)$$

In eqn (9), E represents the total energy, V_0 the equilibrium volume, and ε the strain load. From eqn (9), the total energy (E) can be expressed as in equation

$$E = E_0 + \frac{V_0}{2}\sum_{i,j=1}^{6} C_{ij}\varepsilon_i\varepsilon_j + O(\varepsilon^3) \quad (10)$$

where E_0 stands for the total energy, V_0 the cell volume in the equilibrium state, and $O(\varepsilon^3)$ represents a third order infinitesimal strain load. The Born criterion, which establishes the condition for mechanical stability, states that the energy associated with a homogeneous deformation under an infinitesimal strain must be positive.[44] In practical terms, the C_{ij} matrix should have positive eigenvalues (λ), aligning with the quadratic form described by Hooke's law. The C_{ij} computed utilizing DFT (C_{ij}^{DFT}) and FF (C_{ij}^{FF}) methods is given in eqn (11) and (12).[45–51]

$$C_{ij}^{DFT} = \begin{pmatrix} 47.29 & 17.69 & 13.96 & -2.35 & 0.0 & 0.0 \\ 17.69 & 47.29 & 13.96 & 2.35 & 0.0 & 0.0 \\ 13.96 & 13.96 & 43.36 & 0.0 & 0.0 & 0.00 \\ -2.35 & 2.35 & 0.0 & 7.57 & 0.0 & 0.00 \\ 0.0 & 0.0 & 0.0 & 0.0 & 7.57 & -2.35 \\ 0.0 & 0.0 & 0.0 & 0.0 & -2.35 & 14.80 \end{pmatrix} \quad (11)$$

$$C_{ij}^{FF} = \begin{pmatrix} 65.15 & 26.75 & 20.05 & -3.34 & 0.0 & 0.0 \\ 26.75 & 65.15 & 13.96 & 3.34 & 0.0 & 0.0 \\ 20.05 & 20.05 & 48.84 & 0.0 & 0.0 & 0.0 \\ -3.34 & 3.34 & 0.0 & 10.37 & 0.0 & 0.0 \\ 0.0 & 0.0 & 0.0 & 0.0 & 10.37 & -3.34 \\ 0.0 & 0.0 & 0.0 & 0.0 & -3.34 & 19.20 \end{pmatrix} \quad (12)$$

All the diagonal components are positive in both C_{ij} matrices and the eigenvalues are $\lambda_1^{DFT} = 9.25$, $\lambda_2^{DFT} = 9.60$, $\lambda_3^{DFT} = 20.32$, $\lambda_4^{DFT} = 34.76$, $\lambda_5^{DFT} = 39.17$ and $\lambda_6^{DFT} = 105.98$ GPa; from the force field method, $\lambda_1^{FF} = 6.88$, $\lambda_2^{FF} = 7.08$, $\lambda_3^{FF} = 15.50$, $\lambda_4^{FF} = 30.09$, $\lambda_5^{FF} = 31.65$, $\lambda_6^{FF} = 76.68$ GPa. Despite the C_{ij} (and consequently the eigenvalues) differences between the values derived from DFT computations and force field based (FF) methods, the $Na_2Mg_3Cl_8$ structure is mechanically stable.

With the C_{ij} elements, the other relevant mechanical magnitudes are computed. Table 3 collects the elastic modulus obtained by the DFT and FF approaches of $Na_2Mg_3Cl_8$ structure. The values of Young modulus (E) are comparable to those of other battery materials.[26] For instance, the bulk, shear and Young modulus of Na_6MgCl_8 amount to 26.57, 15.00 and 42.86 GPa, respectively, as reported in ref. 26. The bulk modulus, which is higher than shear modulus, indicates that $Na_2Mg_3Cl_8$ is more susceptible to shape deformation than volume change. In addition, the Young's modulus is higher than the bulk modulus, indicating that $Na_2Mg_3Cl_8$ is better against uniaxial compression or tension than hydrostatic pressure. The $Li_{10}GeP_2S_{12}$ compound, which is used as an SSE in Li-ion batteries, has a Young's modulus of 37.20 GPa.[52] The reported values of other Na-containing materials such as Na_3OBr and Na_3OCl of 55.70 and 60.50 GPa, respectively, are slightly larger.[53] Overall, $Na_2Mg_3Cl_8$ can be regarded as a promising SSE improving the contact with the electrodes.

The bulk (B), shear (G) and Young's (E) modulus derived by DFT computations are smaller than those obtained from the force field-based method. DFT computation tends to underestimate the mechanical properties.[39] With the lack of experimental studies concerning the mechanical properties of this compounds, we would suggest considering these values as both lower and upper bounds. Despite the difference, the B/G ratio derived from both methods are similar to each other. According to Pugh's criteria, it can be noted that the B/G ratio is greater than 1.75, implying that $Na_2Mg_3Cl_8$ is a ductile material, which can deform significantly under stress or when subjected to external forces without cracking.

In order to further explore the elastic anisotropy, the anisotropy regarding compressibility (A_B) and shear (A_G) is defined by eqn (13)

$$A_B = \frac{B_{Voigt} - B_{Reuss}}{B_{Voigt} + B_{Reuss}};\ A_G = \frac{G_{Voigt} - G_{Reuss}}{G_{Voigt} + G_{Reuss}} \quad (13)$$

Table 3 Mechanical properties (in GPa) of the $Na_2Mg_3Cl_8$ structure computed using DFT and FF approaches

Mechanical properties	Method	Reuss	Voigt	Hill
Bulk (B)	DFT	25.33	25.46	25.40
	FF	33.69	34.76	34.22
Shear (G)	DFT	10.36	12.14	11.25
	FF	13.47	15.48	14.47
Young (E)	DFT	37.45	37.45	37.36
	FF	48.97	48.97	40.09
B/G	DFT	2.45	2.10	2.26
	FF	2.50	2.25	2.36
Universal anisotropy (A^U)	DFT	0.87		
	FF	0.78		
A_B	DFT	0.0027		
	FF	0.0157		
A_G	DFT	0.0795		
	FF	0.0692		

for nanocrystalline samples. In eqn (13), a 100% value of both magnitudes corresponds to anisotropy, while a zero value corresponds to elastic isotropy.[54] The A_B and A_G values are both near zero, indicating that the $Na_2Mg_3Cl_8$ compound has elastic isotropy, as confirmed by the low values of universal anisotropy factor A^U defined in eqn (14).[54]

$$A^U = 5(G_{Voigt}/G_{Reuss}) + (B_{Voigt}/B_{Reuss}) - 6 \quad (14)$$

In summary, the $Na_2Mg_3Cl_8$ compound is determined to be mechanically stable and suitable for practical application as solid-state electrolyte.

3.4 Estimation of open cell voltage and capacity of $Na_2Mg_3Cl_8$

To investigate the impact of Na vacancy concentration on the stability of the $Na_2Mg_3Cl_8$ lattice structure, the distribution of sodium vacancies and their energetic cost were investigated. For this purpose, various distributions of sodium vacancies were generated maintaining inequivalent configurations within a $1 \times 2 \times 1$ $Na_2Mg_3Cl_8$ supercell. This study focuses on intermediate compositions of $Na_xMg_3Cl_8$, with x ranging from 0 to 2.0. The site occupancy disorder (SOD) code was used to identify these configurations.[55,56] This approach, which was effective in earlier studies,[57] helps us describe how the Na^+ ions are distributed over the crystal sites.[55–57]

The process begins by generating all possible configurations within the supercell, each uniquely defined by specifying substitution sites in a parent structure. We then select and fully relax the atomic positions and volume of the inequivalent configurations from the complete canonical ensemble. Configurations are considered equivalent if an isometric transformation can convert one into the other.

The symmetry group of the parent structure and internal translations within the supercell provide a list of potential symmetry operations. To evaluate the thermodynamic stability of the pseudo-binary phases of $Na_xMg_3Cl_8$, we used the above-hull energy.[58] All computational analyses, including the construction of phase diagrams, were performed with the Python Materials Genomics (pymatgen) software library.[59] This comprehensive approach allows an in-depth exploration of the thermodynamic landscape to be carried out, thus aiding with the identification of stable compositions and phases under different conditions.

The outstanding stability of the solid electrolyte materials is based on the widely reported electrochemical window of 0–5 V from cyclic voltammetry measurements. Solid electrolyte materials have a limited intrinsic electrochemical window, and the decomposition of most solid electrolyte materials is thermodynamically, favorable the formation of decomposition interphases. In solid electrolytes, stable phases can exist at intermediate ion concentrations that include ion-vacancy orderings in intercalation materials or different atomic orderings in alloys. Atomistic simulations can be used to determine all possible intermediate phases employing the convex hull formalism. However, the number of potential combinations to generate ion vacancies is quite large, making it impractical to be evaluated using atomistic simulations.[58]

The intermediate phases in the system share the same host structure, where sodium ions and vacancies occupy a common sublattice. Addressing the general problem of determining the distribution of Na-vacancy over the available lattice sites can be effectively achieved using the SOD approach, which identifies inequivalent configurations and significantly reduces the number of required calculations.[55]

Fig. 3 depicts the formation energies calculated using an FF-based method for the pseudo-binary phases of $Na_2Mg_3Cl_8$ at temperatures of 0 and 300 K.

At both temperatures, $Na_2Mg_3Cl_8$ and the derivative Mg_3Cl_8 without Na are identified as stable phases, indicated by the blue points on the convex hull. The intermediate compositions are unstable, as represented by red squares above the convex hull (Fig. 3). The formation of intermediate phases is energetically unfavorable. The consistent stability of $Na_2Mg_3Cl_8$ and Mg_3Cl_8 is crucial for their use as solid electrolytes in Na-ion battery.

The stability window is determined by the voltages at which Na^+ is extracted from the electrolyte to form an Na-deficient

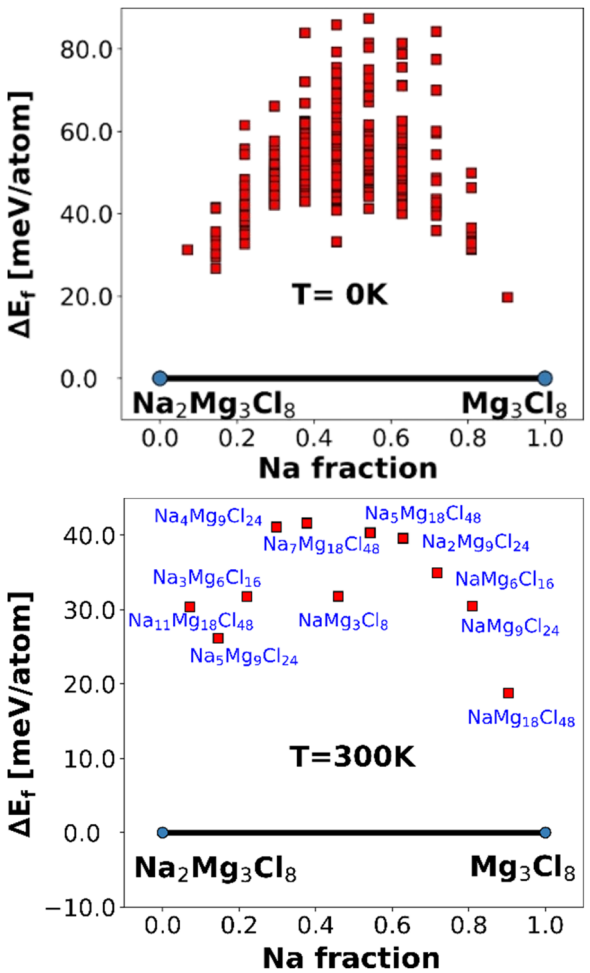

Fig. 3 Formation energies of pseudo-binary phases of $Na_2Mg_3Cl_8$ at 0 (top) and 300 K (bottom). The red point represents the unstable phases in Na^+ vacancy generation.

decomposition layer between the electrolyte and the cathode and at which sodium atom is inserted into the electrolyte, reducing another species and forming an Na-reduced decomposition layer. The open cell voltage (V_{OC}) is an essential magnitude to determine the electrochemical window of the solid-state electrolyte.[1–5] The V_{OC} is estimated by the difference in the chemical potentials of Na^+ ions in the cathode (μ_{cath}^{NA}) and the anode (μ_{an}^{NA}), as described by eqn (15):[20,21]

$$V_{OC} = \frac{\mu_{cath}^{Na} - \mu_{an}^{Na}}{F} \quad (15)$$

where F represents the Faraday's constant, and μ_{cath}^{NA} and μ_{an}^{NA} are the chemical potentials of the cathode and anode, respectively. Combining the Nernst relation with eqn (3), the open cell voltage can be computed in terms of total energy, as described in eqn (16).[20,21]

$$V_{OC} = -\Delta E/xF \quad (16)$$

To assess the energetic cost of an Na-intercalation and the change in the internal energy of the $Na_2Mg_3Cl_8$ structure, a $1 \times 2 \times 1$ supercell of $Na_2Mg_3Cl_8$ was used to remove Na^+-ions, and the total energy was obtained through FF calculations. The change in the reaction energy (ΔE_{Na}) of Na^+ intercalation between both stable phases $Na_2Mg_3Cl_8$ and Mg_3Cl_8 can be calculated using eqn (17).

$$\Delta E_{Na} = E(Na_2Mg_3Cl_8) - [E(Mg_3Cl_8) + 2E(Na)] \quad (17)$$

In addition, predictions of the theoretical capacity (Q) can be done using the Faraday equation

$$Q = zFn/3.6M \quad (18)$$

where n and z represent the number and valence of Na^+ ion, respectively; M is the molar mass of $Na_2Mg_3Cl_8$ and 3.6 is the conversion factor. The computed open cell voltage is 1.18 V, and the theoretical capacity is 133 mA h g^{-1}. The open cell voltage is not a common parameter of interest for solid-state electrolytes. Other properties such as the conductivity at room temperature, mechanical stability, and energy gap are more important for determining the performance of the solid-state electrolyte.[1–5] For instance, the energy gap is more essential than open cell voltage, providing the upper limit for the electrochemically stable region.[1–10] In addition, while a high voltage cathode operates at ~4 V, a band gap slightly superior to 4 eV is more suitable for use as a solid state electrolyte.[1–8]

3.5. Transport properties of $Na_2Mg_3Cl_8$ structure

Knowledge on the diffusion and conduction of alkali ions in a material is crucial when evaluating its potential.[1–14,32,60] The sodium diffusion coefficient and conductivity within the electrode/electrolyte material directly impact the sodiation/desodiation rate during the charge and discharge cycles.[1–14,32,60] The transport properties of candidate materials are essential for picking the one that achieves a high power output, energy density, and long cycle life in Na-ion batteries.[1–14,32,60]

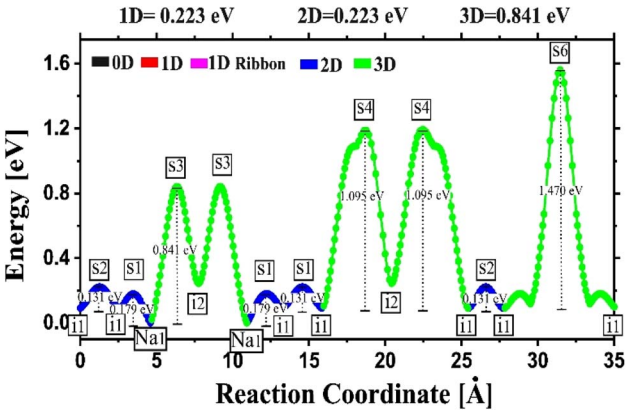

Fig. 4 Energy *vs.* reaction coordinate profile of the $Na_2Mg_3Cl_8$ structure derived from BV computations.

For this purpose, the BVSE was used for prompt predictions of Na^+ transport properties in the $Na_2Mg_3Cl_8$ structure. The first step in a BVSE approach that deals with an exploration of the migration path derived from the BVSE. Migration pathways for Na^+ ions were determined by identifying the regions with low bond valence site energy within mesh grids of $Na_2Mg_3Cl_8$ structure with a resolution of ± 0.1 Å^3.[61]

Fig. 4 depicts the energy profile against the reaction coordinates of the $Na_2Mg_3Cl_8$ structure derived from BVSE computations. Archives containing the BVSE results are included in the ESI.† The respective energy landscape in $Na_2Mg_3Cl_8$ is displayed in Fig. 5a. There are two intermediate sites denoted as i1 and i2, with minimum energies and six transition structures (saddle points labelled with s) with maximum energies, which determine the energy barriers. From Fig. 4 and the energy profile displayed in Fig. 5a, it can be noted that 2D migration paths located between the $[MgCl_6]$ octahedron is the predominant Na^+ ion mechanism in $Na_2Mg_3Cl_8$ with low migration energy barrier. The Na^+ ion migration scheme can be explained by a Na^+ interstitial mechanism: $Na_{Na}^{\times} \rightarrow V_{Na}^{'} + Na_i^{\cdot}$.

Fig. 5b and c collect the transport properties (diffusivity and conductivity) of $Na_2Mg_3Cl_8$ in the temperature range of 300–700 K. An Arrhenius dependence of Na^+ diffusivity and conductivity is observed. The conductivity data was obtained using the Nernst–Einstein equation, where the diffusion coefficient at each temperature is directly related to the Na^+ ion conductivity.[20,21,32]

The calculated activation energy amounts to 0.22 and 0.18 eV for Na^+ diffusion and conduction, respectively. The predicted results of activation energy suggests that there are effective jumps in the mass transport that contribute to the charge transport process, thus lowering the conduction activation energy. Low activation energy in a solid-state electrolyte significantly enhances ionic conductivity, which in turn boosts battery performance by enabling faster charge and discharge rates, improving energy efficiency, and extending the overall lifespan of the battery.[1–10] This leads to more reliable and high-performing energy storage solutions, which crucial for applications ranging from portable electronics to electric vehicles and grid storage systems.[1–11]

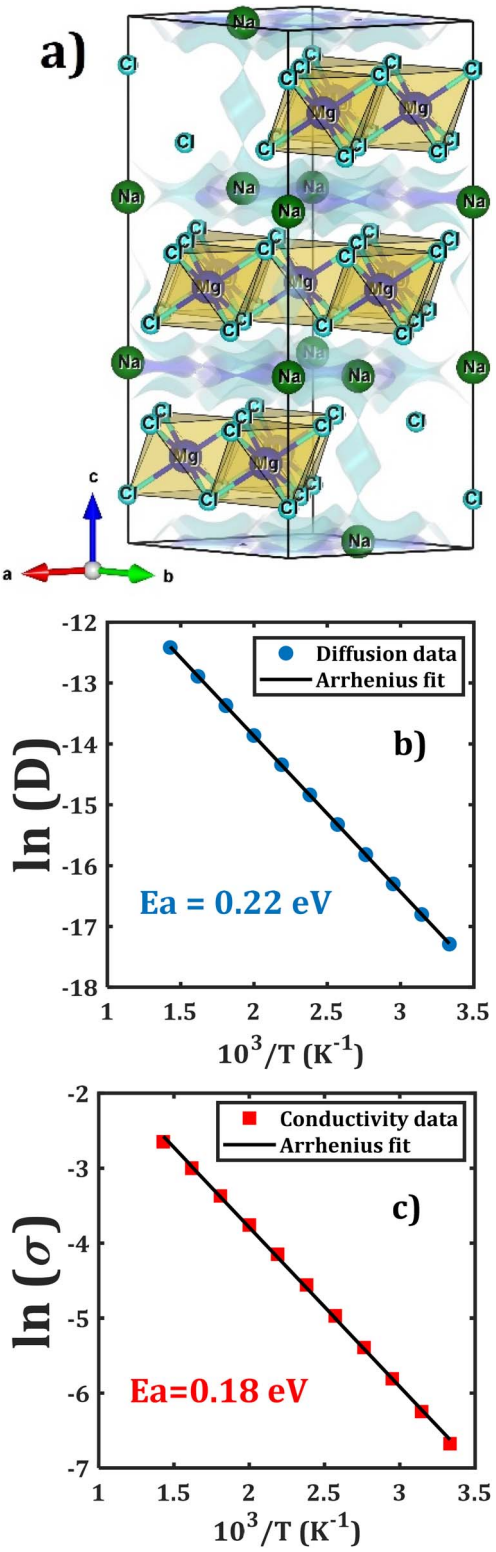

Fig. 5 (a) Bond valence energy landscape in the $Na_2Mg_3Cl_8$ structure (blue isosurfaces) calculated using BVSE and an Arrhenius plot for Na^+; (b) diffusion and (c) conduction in the Na_6MgCl_8 structure.

Together with the low activation energies for diffusion and conduction, the $Na_2Mg_3Cl_8$ structure possesses promising diffusion coefficient and conductivity at 300 K of 3.10×10^{-8} $cm^2\ s^{-1}$ and 1.26 mS cm^{-1}, respectively. The source of these outstanding properties can be explained by the crystal structure of $Na_2Mg_3Cl_8$, specifically by the [NaCl] and [$MgCl_4$] frameworks. As was mentioned in Section 3.1, $Na_2Mg_3Cl_8$ has more Na^+ accessible sites, favoring the migration through interstitial mechanism. The values of activation energy and transport properties at 300 K are equally comparable to those of the currently used solid state electrolytes in Na-ion battery technologies.[62–67] For instance, in a recent study on Na_3YBr_6 solid-state electrolyte, which was prepared *via* a solid-state reaction, has an activation energy of 0.15 eV and promising electrochemical window, making this Na halide compound a good candidate for sodium all solid-state batteries.[68] Another study on the tetragonal phase of Na_3SbS_4 (293–453 K) showed an activation energy of 0.22 eV and conductivity at 293 K of 0.6 mS cm^{-1}.[69] Recent advances significantly improved the room-temperature ionic conductivity of $Na_{1+x}Zr_2Si_xP_{3-x}O_{12}$ ($0 < x < 3$) superionic conductors, reaching a remarkable value of 1 mS cm^{-1}.[70–75] The computed values of room-temperature conductivity and activation energy are competitive with those reported in current SSEs.

In this context, the $Na_2Mg_3Cl_8$ compound, with its remarkably low activation energy of 0.18 eV and impressive room temperature conductivity of 1.26 mS cm^{-1}, stands out as an exceptional candidate for solid-state electrolytes in both current and future Na-ion batteries. We are optimistic that the outstanding properties predicted in this theoretical study will motivate experimental synthesis efforts, paving the way for groundbreaking advancements in $Na_2Mg_3Cl_8$ compounds and their applications in energy storage technologies.

4. Concluding remarks

Advanced atomistic computations were employed to investigate the structural, electronic, mechanical, and transport properties of an unexplored chloride compound, specifically $Na_2Mg_3Cl_8$. The computed lattice parameters using density functional theory and force-field based methods closely match the values reported in the literature. The exploration of electronic properties reveals that the $Na_2Mg_3Cl_8$ structure exhibits insulating characteristics, with an energy gap of ~4.9 eV arising from the hybridization of [NaCl] trigonal prismatic and [$MgCl_6$] octahedral units.

The exploration of mechanical properties points out that $Na_2Mg_3Cl_8$ is a ductile material and mechanically stable, which is beneficial for practical fabrication, improving the electrolyte/electrode contact, reducing the resistance and improving the performance of the battery device. On the other hand, $Na_2Mg_3Cl_8$ has appropriate transport properties with low activation energies for both diffusion and conduction processes and an outstanding room-temperature conductivity of 1.26 mS cm^{-1} comparable to that of other superionic conductors.

In light of these remarkable properties, experimental synthesis efforts are highly desirable to validate our theoretical predictions regarding the $Na_2Mg_3Cl_8$ compound as a solid electrolyte.

Data availability

The data supporting this article have been included as part of the ESI.†

Author contributions

YAZ: conception, data acquisition and interpretation, original draft preparation, editing, review. JRFG: data acquisition and interpretation, original draft preparation. TVBP: funding, editing, review. MPPH: data analysis, editing, review. MTN: conception, project supervision, manuscript editing and review. All authors reviewed the manuscript.

Conflicts of interest

There are no conflicts to declare.

Acknowledgements

The authors acknowledge the support provided by the VinUniversity Center for Environmental Intelligence under Flagship Project VUNI.CEI.FS_0005. MTN thanks Van Lang University and MPPH acknowledges the Ho Chi Minh City University of Technology (HCMUT) and VNU-HCM for support.

Notes and references

1 Y. Deng, C. Eames, L. H. B. Nguyen, O. Pecher, K. J. Griffith, M. Courty, B. Fleutot, J. N. Chotard, C. P. Grey, M. S. Islam and C. Masquelier, *Chem. Mater.*, 2018, **30**, 2618–2630.
2 H. Tian, S. Liu, L. Deng, L. Wang and L. Dai, *Energy Storage Mater.*, 2021, **39**, 232–238.
3 K. Chayambuka, G. Mulder, D. L. Danilov and P. H. L. Notten, *Adv. Energy Mater.*, 2018, **8**, 1–49.
4 B. Singh, Z. Wang, S. Park, G. S. Gautam, J. N. Chotard, L. Croguennec, D. Carlier, A. K. Cheetham, C. Masquelier and P. Canepa, *J. Mater. Chem. A*, 2021, **9**, 281–292.
5 Y. Wang, S. Song, C. Xu, N. Hu, J. Molenda and L. Lu, *Nano Mater. Sci.*, 2019, **1**, 91–100.
6 A. Emly, E. Kioupakis and A. Van Der Ven, *Chem. Mater.*, 2013, **25**, 4663–4670.
7 J. Xu, Y. Wang, S. Wu, Q. Yang, X. Fu, R. Xiao and H. Li, *ACS Appl. Mater. Interfaces*, 2023, **15**, 21086–21096.
8 B. Tao, D. Zhong, H. Li, G. Wang and H. Chang, *Chem. Sci.*, 2023, **14**, 8693–8722.
9 Z. Wei, L. F. Nazar and J. Janek, *Batteries Supercaps*, 2024, **7**, e202400005.
10 Q. Zhao, S. Stalin, C. Z. Zhao and L. A. Archer, *Nat. Rev. Mater.*, 2020, **5**, 229–252.
11 M. Armand and J. M. Tarascon, *Nature*, 2008, **451**, 652–657.
12 Q. Ma and F. Tietz, *ChemElectroChem*, 2020, **7**, 2693–2713.
13 H. Ahmad, K. T. Kubra, A. Butt, U. Nisar, F. J. Iftikhar and G. Ali, *J. Power Sources*, 2023, **581**, 233518.
14 N. Aslfattahi, L. Samylingam, M. S. Kiai, K. Kadirgama, V. Kulish, M. Schmirler and Z. Said, *J. Energy Storage*, 2023, **72**, 108781.
15 A. A. Franco, A. Rucci, D. Brandell, C. Frayret, M. Gaberscek, P. Jankowski and P. Johansson, *Chem. Rev.*, 2019, **119**, 4569–4627.
16 L. L. Wong, K. C. Phuah, R. Dai, H. Chen, W. S. Chew and S. Adams, *Chem. Mater.*, 2021, **33**, 625–641.
17 S. Adams, *Solid State Ionics*, 2006, **177**, 1625–1630.
18 I. D. Brown, *Chem. Rev.*, 2009, **109**, 6858–6919.
19 H. Chen, L. L. Wong and S. Adams, *Acta Crystallogr., Sect. B: Struct. Sci., Cryst. Eng. Mater.*, 2019, **75**, 18–33.
20 Y. A. Zulueta and M. T. Nguyen, *Phys. Chem. Chem. Phys.*, 2023, **25**, 27926–27935.
21 Y. A. Zulueta and M. T. Nguyen, in *Annual Reports in Computational Chemistry*, Elsevier, 2023, vol. 19, pp. 1–43.
22 J. Sung, J. Heo, D.-H. Kim, S. Jo, Y.-C. Ha, D. Kim, S. Ahn and J.-W. Park, *Mater. Chem. Front.*, 2024, **8**, 1861–1887.
23 X. Nie, J. Hu and C. Li, *Interdiscip. Mater.*, 2023, **2**, 365–389.
24 C. Fu, Y. Li, W. Xu, X. Feng, W. Gu, J. Liu, W. Deng, W. Wang, A. M. M. Abeykoon, L. Su, L. Zhu, X. Wu and H. Xiang, *Nat. Commun.*, 2024, **15**, 4315.
25 Y. A. Zulueta, M. P. Pham-Ho and M. T. Nguyen, *RSC Adv.*, 2024, **14**, 21644–21652.
26 Y. A. Zulueta, M. P. Pham-Ho and M. T. Nguyen, *J. Phys. Chem. Solids*, 2024, **188**, 111916.
27 C. J. J. Loon and D. J. W. Ijdo, *Acta Crystallogr., Sect. B: Struct. Crystallogr. Cryst. Chem.*, 1975, **31**, 770–773.
28 M. C. Payne, M. P. Teter, D. C. Allan, T. A. Arias and J. D. Joannopoulos, *Rev. Mod. Phys.*, 1992, **64**, 1045–1097.
29 D. Vanderbilt, *Phys. Rev. B: Condens. Matter Mater. Phys.*, 1990, **41**, 7892–7895.
30 H. J. Monkhorst and J. D. Pack, *Phys. Rev. B: Solid State*, 1976, **13**, 5188–5192.
31 J. D. Gale and A. L. Rohl, *Mol. Simul.*, 2003, **29**, 291–341.
32 B. A. Goldmann, M. J. Clarke, J. A. Dawson and M. S. Islam, *J. Mater. Chem. A*, 2022, **10**, 2249–2255.
33 *Computational Modelling of Zinc Oxide and Related Oxide Ceramics*, University of Surrey, **https://openresearch.surrey.ac.uk/esploro/outputs/doctoral/Computational-Modelling-of-Zinc-Oxide-and/99512944702346**, (accessed 30 May 2024).
34 B. G. Dick and A. W. Overhauser, *Phys. Rev.*, 1958, **112**, 90–103.
35 N. F. Mott and M. J. Littleton, *Trans. Faraday Soc.*, 1938, **34**, 485–499.
36 J. D. Gale, *J. Chem. Soc., Faraday Trans.*, 1997, **93**, 629–637.
37 L. Van Duong, M. T. Nguyen and Y. A. Zulueta, *RSC Adv.*, 2022, **12**, 20029–20036.
38 L. L. Wong, K. C. Phuah, R. Dai, H. Chen, W. S. Chew and S. Adams, *Chem. Mater.*, 2021, **33**, 625–641.
39 M. G. Medvedev, I. S. Bushmarinov, J. Sun, J. P. Perdew and K. A. Lyssenko, *Science*, 2017, **355**, 49–52.
40 F. A. Kröger, *The Chemistry of Imperfect Crystals*, North-Holland Pub. Co., 1964.
41 Z. Ding, J. Li, J. Li and C. An, *J. Electrochem. Soc.*, 2020, **167**, 070541.
42 X. Ke, Y. Wang, G. Ren and C. Yuan, *Energy Storage Mater.*, 2020, **26**, 313–324.

43 M. Hou, F. Liang, K. Chen, Y. Dai and D. Xue, *Nanotechnology*, 2020, **31**, 132003.
44 M. Born, K. Huang and M. Lax, *Am. J. Phys.*, 1955, **23**, 474.
45 I. N. Frantsevich, F. F. Voronov and S. A. Bokuta, *Elastic Constants and Elastic Moduli of Metals and Insulators Handbook*, Naukova Dumka, Kiev, 1983, pp. 60–180.
46 F. I. Fedorov, *Theory of Elastic Waves in Crystals*, Springer US, Boston, MA, 1968.
47 W. Voigt *Lehrbuch der Kristallphysik (BG Teubner Leipzig und 791 Berlin) 980 S; Reproduced 1966 Spring Fachmedien Wiesbaden GmbH*, 1928.
48 A. Reuss, *J. Appl. Math. Mech.*, 1929, **9**, 49–58.
49 R. Hill, *Proc. Phys. Soc., London, Sect. A*, 1952, **65**, 349–354.
50 R. Hill, *J. Mech. Phys. Solids*, 1963, **11**, 357–372.
51 S. F. Pugh, *London, Edinburgh Dublin Philos. Mag. J. Sci.*, 1954, **45**, 823–843.
52 Z. Q. Wang, M. S. Wu, G. Liu, X. L. Lei, B. Xu and C. Y. Ouyang, *Int. J. Electrochem. Sci.*, 2014, **9**, 562–568.
53 M. A. Sattar, M. Javed, M. Benkraouda and N. Amrane, *Int. J. Energy Res.*, 2021, **45**, 4793–4810.
54 S. I. Ranganathan and M. Ostoja-Starzewski, *Phys. Rev. Lett.*, 2008, **101**, 055504.
55 R. Grau-Crespo, S. Hamad, C. R. A. Catlow and N. H. d. Leeuw, *J. Phys.: Condens. Matter*, 2007, **19**, 256201.
56 V. Fotopoulos, R. Grau-Crespo and A. L. Shluger, *Phys. Chem. Chem. Phys.*, 2023, **25**, 9168–9175.
57 J. R. Fernández-Gamboa, F. Tielens and Y. A. Zulueta, *Mater. Sci. Semicond. Process.*, 2024, **173**, 108144.
58 C. J. Bartel, *J. Mater. Sci.*, 2022, **57**, 10475–10498.
59 S. P. Ong, W. D. Richards, A. Jain, G. Hautier, M. Kocher, S. Cholia, D. Gunter, V. L. Chevrier, K. A. Persson and G. Ceder, *Comput. Mater. Sci.*, 2013, **68**, 314–319.
60 J. Zhu, Y. Wang, S. Li, J. W. Howard, J. Neuefeind, Y. Ren, H. Wang, C. Liang, W. Yang, R. Zou, C. Jin and Y. Zhao, *Inorg. Chem.*, 2016, **55**, 5993–5998.
61 J. Liang, X. Li, S. Wang, K. R. Adair, W. Li, Y. Zhao, C. Wang, Y. Hu, L. Zhang, S. Zhao, S. Lu, H. Huang, R. Li, Y. Mo and X. Sun, *J. Am. Chem. Soc.*, 2020, **142**, 7012–7022.
62 N. Wang, K. Yang, L. Zhang, X. Yan, L. Wang and B. Xu, *J. Mater. Sci.*, 2018, **53**, 1987–1994.
63 Q. Zhang, C. Zhang, Z. D. Hood, M. Chi, C. Liang, N. H. Jalarvo, M. Yu and H. Wang, *Chem. Mater.*, 2020, **32**, 2264–2271.
64 R. Jalem, A. Hayashi, F. Tsuji, A. Sakuda and Y. Tateyama, *Chem. Mater.*, 2020, **2020**, 58.
65 X. Y. Niu, X. Y. Dou, C. Y. Fu, Y. C. Xu and X. Y. Feng, *RSC Adv.*, 2024, **14**, 14716–14721.
66 J. A. Dawson, T. S. Attari, H. Chen, S. P. Emge, K. E. Johnston and M. S. Islam, *Energy Environ. Sci.*, 2018, **11**, 2993–3002.
67 L. Wang, Z. Song, X. Lou, Y. Chen, T. Wang, Z. Wang, H. Chen, W. Yin, M. Avdeev, W. H. Kan, B. Hu and W. Luo, *Small*, 2024, 2400195.
68 X. Y. Niu, X. Y. Dou, C. Y. Fu, Y. C. Xu and X. Y. Feng, *RSC Adv.*, 2024, **14**, 14716–14721.
69 R. Jalem, A. Hayashi, F. Tsuji, A. Sakuda and Y. Tateyama, *Chem. Mater.*, 2020, **32**, 8373–8381.
70 J. Luo, G. Zhao, W. Qiang and B. Huang, *J. Am. Ceram. Soc.*, 2022, **105**, 3428–3437.
71 J. F. Nonemacher, S. Naqash, F. Tietz and J. Malzbender, *Ceram. Int.*, 2019, **45**, 21308–21314.
72 B. Hitesh and A. Sil, *J. Am. Ceram. Soc.*, 2023, **106**, 6743–6754.
73 Z. Gao, J. Yang, G. Li, T. Ferber, J. Feng, Y. Li, H. Fu, W. Jaegermann, C. W. Monroe and Y. Huang, *Adv. Energy Mater.*, 2022, **12**, 2103607.
74 E. J. Cheng, T. Yang, Y. Liu, L. Chai, R. Garcia-Mendez, E. Kazyak, Z. Fu, G. Luo, F. Chen, R. Inada, V. Badilita, H. Duan, Z. Wang, J. Qin, H. Li, S. Orimo and H. Kato, *Mater. Today Energy*, 2024, **44**, 101644.
75 N. Wang, K. Yang, L. Zhang, X. Yan, L. Wang and B. Xu, *J. Mater. Sci.*, 2018, **53**, 1987–1994.